IEEE Photonics Journal
An IEEE Photonics Society Publication

Open Access

Tip/tilt Alignment for a Fizeau Interferometer via Defocus-Based Sub-Spot Separation

Volume 12, Number 6, December 2020

Wenyi Lv
Zongliang Xie
Qiang Wang
Haotong Ma
Jianliang Shi
Yang Liu
Kaiyuan Yang
Botao Chen
Yongmei Huang

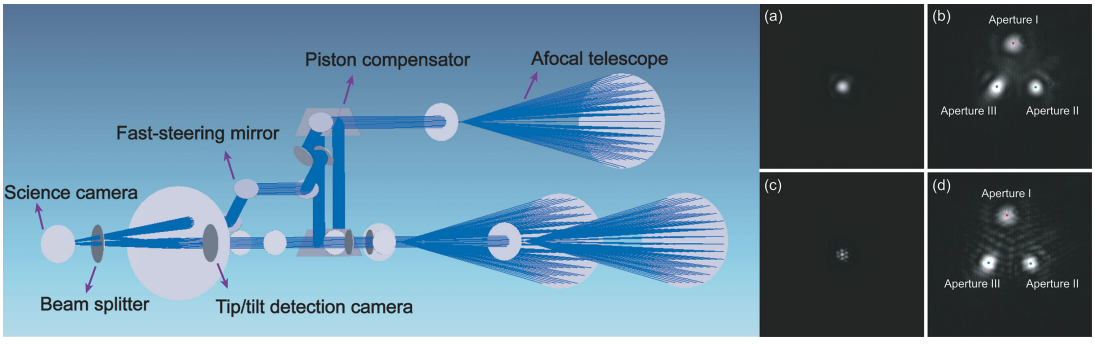

DOI: 10.1109/JPHOT.2020.3032524

Tip/tilt Alignment for a Fizeau Interferometer via Defocus-Based Sub-Spot Separation

Wenyi Lv,[1,2,3] **Zongliang Xie**,[1,2,3] **Qiang Wang**,[1,2,3] **Haotong Ma**,[1,2,3] **Jianliang Shi**,[1,2,3] **Yang Liu**,[1,2,3] **Kaiyuan Yang**,[1,2,3] **Botao Chen**,[1,2,3] **and Yongmei Huang**[1,2,3]

[1]Key Laboratory of Optical Engineering, Chinese Academy of Science, Chengdu 61020, China
[2]Institute of Optics and Electronics, Chinese Academy of Science, Chengdu 61020, China
[3]University of Chinese Academy of Science, Beijing 100049, China

DOI:10.1109/JPHOT.2020.3032524

Manuscript received October 12, 2020; accepted October 15, 2020. Date of publication October 20, 2020; date of current version November 3, 2020. This work was supported in part by the National Natural Science Foundation of China (62005289), in part by the Open Research Fund of State Key Laboratory of Pulsed Power Laser Technology (SKL2018KF05), in part by the Excellent Youth Foundation of Sichuan Scientific Committee (2019JDJQ0012), in part by the Youth Innovation Promotion Association, CAS (2018411, 2020372), and in part by the CAS "Light of West China" Program and the Young Talents of Sichuan Thousand People Program. Corresponding authors: Zongliang Xie; Yongmei Huang (e-mail: zongliang.xie@yahoo.com; huangym@ioe.ac.cn).

Abstract: It is a crucial premise for Fizeau interferometric imaging that all the optical axes of sub-apertures are well aligned. What is challenging in tip/tilt alignment of such interferometers is the superposition of all the sub-aperture spots on the focal plane for generation of fringes. In this paper, we propose and demonstrate a simple tip/tilt alignment scheme via defocus-based sub-spot separation (TADS). The focal interference function is divided into sparse defocused sub-spots at a long defocusing distance. Then the servo-control technology with a centroid extracting algorithm is used to align all the sub-aperture optical axes, each corresponding to a defocused sub-spot. The pointing correction performance using TADS has been verified through closed-loop experiments performed on a Fizeau telescope array testbed newly built in our laboratory. Compared with the current means, the proposed TADS eliminates the requirement of complex hardware design and the limitation of sub-aperture amounts, which is compatible with most existing segmented mirrors and telescope arrays.

Index Terms: Fizeau interferometric imaging, tip/tilt alignment, servo-control technology.

1. Introduction

According to the Rayleigh criterion, high-resolution optical imaging systems, such as space-based telescopes, require large apertures for distinguishing distant objects. However, due to the mass, volume and cost constraints, unlimited increase of the aperture size is impossible. To overcome these restrictions, current trends are to develop segmented primary mirror telescopes and phased telescope arrays adopting the principle of Fizeau interferometry.

The segmented primary mirror is a mosaic of multiple small mirrors. Keck I and Keck II telescopes with 10 m diameter primary mirror are composed of 36 hexagonal segments [1], [2]. Large

terrestrial telescopes under construction commonly employ the form of the segmented primary mirror such as TMT [3], ELT [4] and GMT [5]. Another notable project is the largest space-based telescope, James Webb Space Telescope (JWST) [6]. Developed by NASA, the primary mirror of JWST is a tiling pattern of 18 hexagonal segments.

The phased telescope array producing interferometric resolvable images by combining all the sub-aperture beams is also of interest for astronomical exploration. So far, many telescope array testbeds have been constructed such as MMT [7], Phasar [8], MMTT [9], ARGOS [10] and Star-9 [11].

For both segmented primary mirror telescopes and phased telescope arrays, sub-aperture patterns each need to be superposed totally and stabilized for the generation of fringes. The peaks of the signal-to-noise ratio (PSNR) decrease when tip/tilt aberrations increase [12]. In other words, the tip/tilt aberrations arising from the air turbulence, the ground vibration, the thermal drift, the carrier jitter or the actuator creep are required to be kept within a certain tolerance. However, the task of pointing correction for Fizeau interferometers is not as easy to perform as that for a single aperture telescope. The tip/tilt can be easily detected from the shifts of the focal spot for a conventional telescope. Instead, since the focal imaging results of the synthetic aperture system is an interferometric superimposition of all sub-aperture spots, it is difficult to extract the tip/tilt of each sub-aperture respectively from the overall variation of the focal intensity. Phase diversity, one of the potential approaches to address the problem [13], is able to estimate wavefront degradation (including the tip/tilt) with a couple of defocused diversity images and nonlinear optimization. The Star-9 has applied the phase diversity for fine phasing [14]. Yet this technique is limited to heavy computational loads owing to the iteration requirement. The rate of phase diversity can only achieve several Hz to several tens Hz [11], [15], [16] despite fast development of the computing hardware. However, impressively, a non-iterative method for large amplitude tip/tilt estimation using pseudo-defocus diversity has been proposed [17], which might be promising for real-time alignment [18]. In projects that require real-time wavefront correction, the strategy commonly employed is designing complex optical modules to spatially separate sub-aperture spots on the detector. For instance, I2T [19]–[21] and Mark III stellar [22] interferometers made use of optical pyramids and annular wedges for light separation, respectively. Recently, FIIT interferometer with three sub-telescopes has designed a pointing correction module consisting of several cube prisms to divide three sub-aperture spots [23]. Tip/tilt alignment technique using additional splitting optics does not only increase the physical complexity of the system, but also suffers from poor portability. For instance, the optical configurations of these beam stabilization modules need to be modified if the sub-aperture number increases.

In this paper, a simple tip/tilt alignment scheme via defocus-based sub-spot separation (TADS) is reported. We propose to use a detector located at a long defocusing position instead of additional optics to perform beam separation. According to the geometrical relations, defocused sub-spots sparsely distributed like the form of the array arrangement are obtained. In this way, the problem of the tip/tilt alignment for a Fizeau interferometer degrades to that for a conventional single-aperture telescope. The tip/tilt of each sub-aperture can be sensed by tracking the shifts of the corresponding defocused sub-spot on a detection camera. Then the servo-control technology combined with a centroid extracting algorithm is utilized to align all the sub-aperture optical axes. We verify the alignment performance of TADS through closed-loop experiments performed on a Fizeau telescope array testbed that we newly build in our laboratory. TADS outperforms previous techniques in two aspects. It is easy to implement without the requirement of complex hardware design. Also, it is irrelevant to the optical configurations, thus being compatible with the existing Fizeau interferometers and having no limitations of the sub-aperture amount.

This paper is structured as follows. The optomechanical design of our Fizeau telescope array testbed is briefly introduced in Section 2. How TADS detects the tip/tilt is presented in Section 3. The servo-control module is described in Section 4. The experimental results of closed-loop tip/tilt alignment are exhibited in Section 5. Section 6 summarizes this paper.

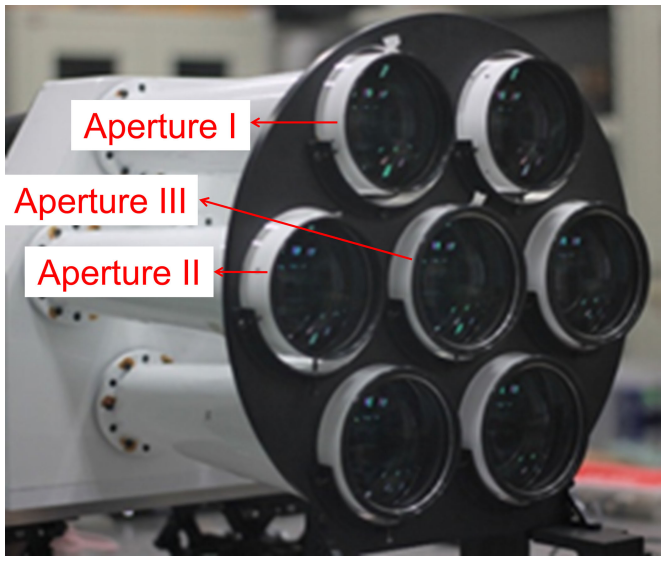

Fig. 1. Front view of the Fizeau telescope array testbed.

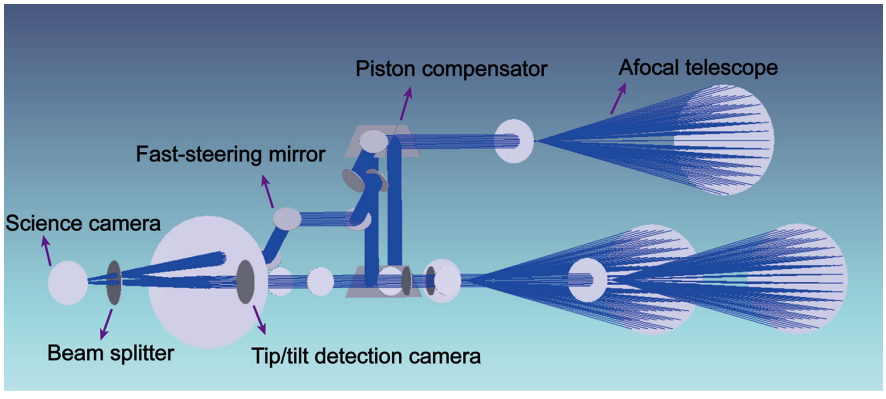

Fig. 2. The overall layout of the three sub-telescopes combination.

2. Optomechanical Design of Fizeau Telescope Array Testbed

For the purpose of investigating the performance of Fizeau interferometric imaging, a telescope array testbed with seven individual sub-telescopes has been built in our laboratory, of which the front view is shown in Fig. 1. The infinite target is simulated by locating a laser light source with the wavelength of 633 nm on the focal plane of a collimator with 300 mm diameter. The testbed consists of seven identical afocal sub-telescopes with the diameter of 100 mm and the angular magnification of 8. As shown in Fig. 1, six sub-telescopes are arranged along a concentric ring around a central one with 145 mm baselines between each other. Currently, due to the limitation of the collimator aperture, three sub-telescopes marked in red in Fig. 1 are selected to verify the performance of TADS, which are referred to as aperture I, aperture II and aperture III. The overall layout of the three sub-telescope combination is illustrated in Fig. 2. Three couples of reflective mirrors mounted on high-precision translation stages are applied for compensating pistons. Three fast steering mirrors (FSMs) perform tip/tilt adjustments. All the sub-aperture beams are focused by a beam combiner with the focal length of 2032 mm.

There are two cameras, one for direct imaging on the focal plane and the other for tip/tilt detection on the defocusing plane. Tip/tilt alignment is the prerequirement of the testbed's phased imaging

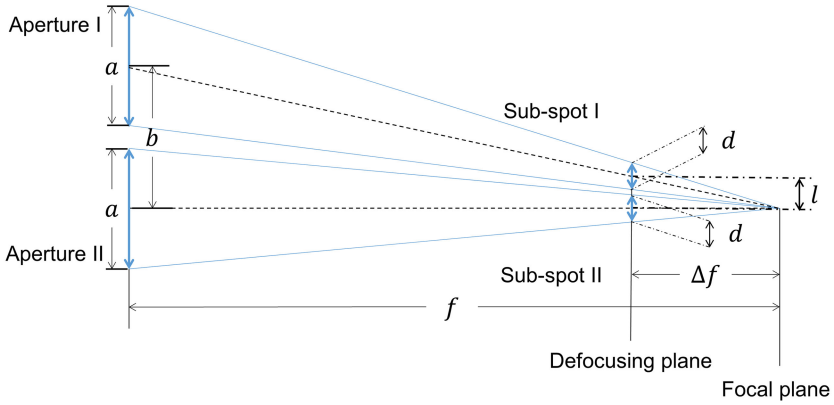

Fig. 3. Schematic diagram of geometric optics for aperture I and aperture II.

and indeed the focus of this paper. It is ongoing to use image-based techniques [24], [25] to sense and correct pistons. More details of the optical design of the seven sub-aperture testbed are also in preparation.

3. Tip/tilt Detecting using TADS

3.1 Defocus-Based Sub-Spot Separation

The light coming from the beam combiner is separated by a beam splitter to fall upon two imaging planes: the focal and defocusing plane. As shown in Fig. 3, which takes two apertures as examples based on geometric optics, to completely separate each sub-spot on the defocusing plane for facilitating the tip/tilt sensing, a geometric condition has to be met that can be obviously expressed as follows:

$$l > d \tag{1}$$

where l presents the center distance between two sub-spots, and d denotes the diameter of two sub-spots. According to the geometric relationships of similar triangles, the diameter of two sub-spots are expressed as:

$$d = \frac{a\Delta f}{f} \tag{2}$$

where a is the diameter of two sub-apertures, Δf is the defocusing length and f is the focal length. Also from the geometric relationship, the distance between two sub-spots is expressed as:

$$l = \frac{b\Delta f}{f} \tag{3}$$

where b is the center distance between two apertures. Substituting Eq. (2) and Eq. (3) into Eq. (1), the condition for ensuring that the sub-spots have no geometric overlap on the defocusing plane is defined as:

$$b > a \tag{4}$$

In fact, even when $b = a$, the sub-spots can be also recognized on a proper defocusing plane. The sub-spots are diffraction patterns with most energy in the central bright regions and little energy distributed around. It is the sub-aperture bright regions that enable the measurements of individual positions, which can be also separated on a proper defocusing plane. As an example, Fig. 4 *shows*

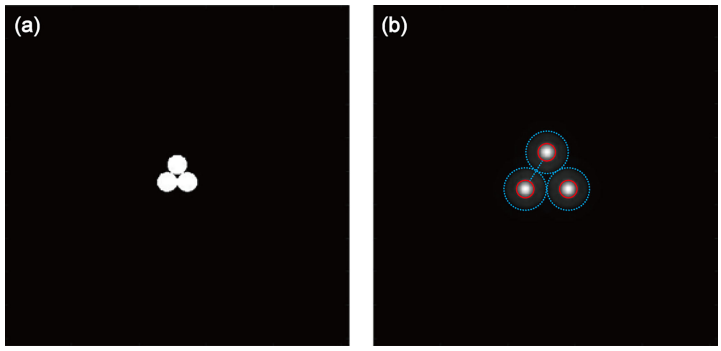

Fig. 4. (a) An ideal system with 3 adjacent sub-apertures and (b) the incoherent intensity distribution on a defocusing plane.

the simulated incoherent intensity distribution on a defocusing plane of an ideal 3 sub-aperture system with $b = a$, where the bright regions marked by red circles are obviously separated. Also, using pupil masks which is common in phasing a multi-aperture system [26], [27] can help separate the sub-spots better.

Since without additional optics, the capture range of TADS is limited. It can be used for fine alignment aimed at correcting small disturbance. If the sub-aperture bright regions overlapped, TADS would fail. Thus, we define the capture range as half the distance between the edges of the two neighboring bright regions, marked with blue dotted lines in Fig. 1. It is flexible to decide the optimal defocusing length in engineering projects. We can conveniently adjust the defocusing length just to let the capture range be the largest, while simultaneously guaranteeing the centroids being extracted stably.

For our telescope array testbed, a is 100 mm and b is 145 mm, which satisfies the Eq. (4). Hence, based on the geometric optics, no matter what the defocusing length is, the sub-spots of our system are separated on the defocusing plane theoretically. However, due to the diffraction of light, the spots are not ideal points but diffracted patterns. Thus, a relatively large defocusing length is required to have all the defocused sub-spots separated.

As shown in Fig. 5(a), three sub-aperture beams are focused on the science camera, converging into one spot. When the piston errors are corrected, interference fringes emerge shown in Fig. 5(c). In this case, it is difficult to sense tip/tilt of each sub-aperture from the superposed focal spot. TADS simply uses a detector located at a long defocusing position instead of additional optics [23] to perform beam separation. On the long defocusing plane, according to the geometrical relations, three sub-spots with and without interference can both be completely separated and sparsely distributed like a regular triangle, as shown in Fig. 5(b) and 5(d), respectively. As a result, the tip/tilt errors of each sub-aperture manifest themselves as lateral shifts of the corresponding defocused sub-spot. In this way, TADS allows tip/tilt of each sub-telescope to be controlled separately without quantity limitation and complex hardware design.

Science and tip\tilt detecting cameras (Baumer's product, HXC20) are the same, with 2048 $\times$ 1088 pixels and 5.5 μm pitch (0.338 microradians). In closed-loop experiments, the frame rate is 100 fps for a window with 512 $\times$ 512 pixels.

3.2 Centroid Extracting Algorithm

Centroid positions of defocused sub-spots calculated by a centroid extracting algorithm characterize the tip/tilt errors. In order to achieve the separation of the target spots and the background, image segmentation is performed first as:

$$g(x, y) = \begin{cases} 255, & f(x, y) \geq Th \\ 0, & f(x, y) < Th \end{cases} \tag{5}$$

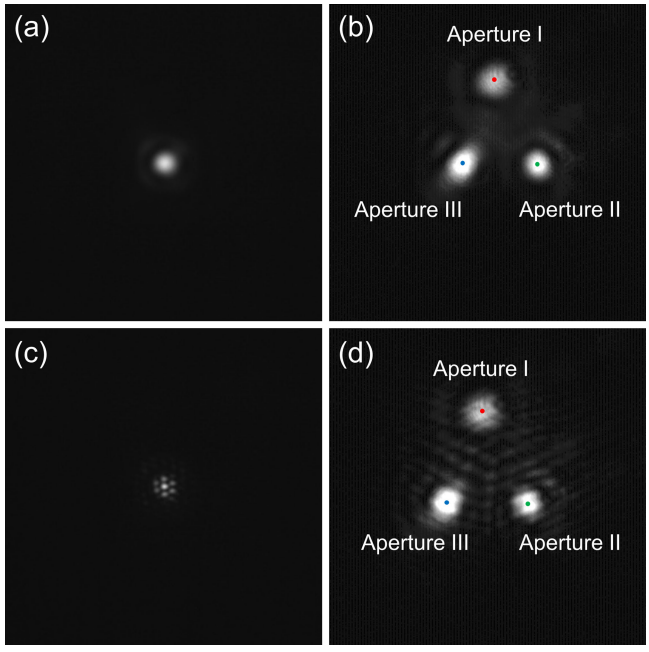

Fig. 5. Images captured by cameras: (a) focused image on the science camera without interference; (b) defocused image on the tip/tilt detection camera without interference; (c) focus image with interference; and (d) the defocused image with interference.

where $g(x, y)$ is the binarized image obtained from image segmentation, $f(x, y)$ is the captured image, and Th is the threshold. The threshold is proportional to the maximum value in the image pixels, expressed as:

$$Th = k \max [f(x, y)] \tag{6}$$

where k is the proportional coefficient ($0 \leq k \leq 1$), which should change with the image quality. The larger the k is, the more pixels are filtered. In the closed-loop experiment in Section 5, the value of k is selected as 0.7.

Image segmentation is a statistical analysis of the gray distribution characteristics of the captured image, which simplifies the processed image. In spite of great reduction of noise after image segmentation, there may still be some isolated noise points, when the optical system is not well calibrated. Besides, the target spots might be divided into several fractured areas due to the image segmentation. Since real targets generally have a certain area, further filtering out the noise points and connecting multiple fractured areas that belong to the same target can increase target recognition probability.

Erosion operation can eliminate the noise points that are smaller than the structuring element, defined as:

$$A \ominus B_e = \left\{ z | (B_e)_z \subseteq A \right\} \tag{7}$$

where A is the target to be eroded, and B_e is erosion structuring element. Dilation operation can connect the regions that are mis-segmented but belong to the same target, defined as:

$$A \oplus B_d = \left\{ z | \left(\hat{B}_d \right)_z \cap A \neq \emptyset \right\} \tag{8}$$

where A is target to be dilated, and B_d is dilation structuring element. When erosion and dilation operators are used in series, and the dilation structuring element is larger than the erosion structuring element, the real target is more completely retained while filtering the noise, shown

as follows:

$$h\ (x, y) = (g\,(x, y) \ominus B_e)\ \oplus B_d \tag{9}$$

where $h(x, y)$ is the filtered image. The size of B_d is selected as 1×2, and the size of B_e is selected as 3×3. When the optical system is well calibrated (as demonstrated in the closed-loop experiment in section 5), the erosion and the dilation operation can be omitted.

After performing the above image segmentation and image filtering, the centroid position of target spots can be calculated by following equations:

$$\bar{x}_i = \frac{\sum_x \sum_y xh\,(x, y)}{\sum_x \sum_y h\,(x, y)} \tag{10}$$

$$\bar{y}_i = \frac{\sum_x \sum_y yh\,(x, y)}{\sum_x \sum_y h\,(x, y)} \tag{11}$$

where $(\bar{x}_i, \bar{y}_i)$ is the centroid position of target spots, and $i = 1, 2, 3$. The accuracy of $(\bar{x}_i, \bar{y}_i)$ reaches sub-pixel level, which is 0.01 pixels.

The centroid positions of target spots are obtained from every frame of captured image. The tip/tilt is characterized by the shifts between the reference position and the current centroid position. The two targets with the closest distance between two adjacent frames are determined as the same one.

However, sometimes the stray light and the occlusion of the spots may cause the centroid extracting algorithm to get an incorrect number of the target spots. Accordingly, a judgment procedure is designed for determining whether the centroid position is effective, which is described as follows:

1) If the number of targets in the filtered image is greater than three, they will be sorted according to the size of the targets, and the first three largest targets will be regarded as the target spots of the current frame;
2) If the number of targets in the filtered image is less than three, the current centroid position is determined to be invalid;
3) If the distance between the same target in the two adjacent frames is greater than the preset threshold, the current centroid position is invalid.

The centroid extracting algorithm does not require high computing resources and can provide accurate centroids regardless of the target spot amount. The algorithm is effective whether the spots interfere with each other or not as shown in Figs. 5(b) and 5(d), where the red, blue and green dots are marked by the algorithm, representing the centroid positions of each sub-spot, respectively. Therefore, it is feasible to obtain the tip/tilt via the centroid extracting algorithm.

Extracting the spot centroids is to provide reference positions for the tip/tilt alignment. What is really important is guaranteeing the reference positions extracted at each frame to be the same. The aberrations caused by manufacture errors, optics calibration, and so on, which preserve the spot shapes during image capture, have no effects on the tip/tilt correction. On the contrary, the aberrations caused by severe atmosphere turbulence, heavy heating effects, and so on, which change the spot shapes during image capture, increase the alignment errors. Then, the adaptive optics might be needed.

4. Servo-Control Module

The servo-control module consists of FSMs, an image processing unit (IPU) and an integrated control unit (ICU). While the tip/tilt detection camera is collecting images, the IPU is working to calculate the centroid positions, and sending the results to the ICU. Due to the rounding errors in data transmission, the accuracy of the centroid positions that the ICU receives is $1/16 = 0.0625$ pixels. The FSMs are controlled by the ICU with a control algorithm. Driven by piezoelectric (PZT) ceramics, the FSMs are able to rotate around two orthogonal axes to align the tip/tilt. The classic feedback control structure for FSMs is illustrated in Fig. 6. The green part is the open-loop control,

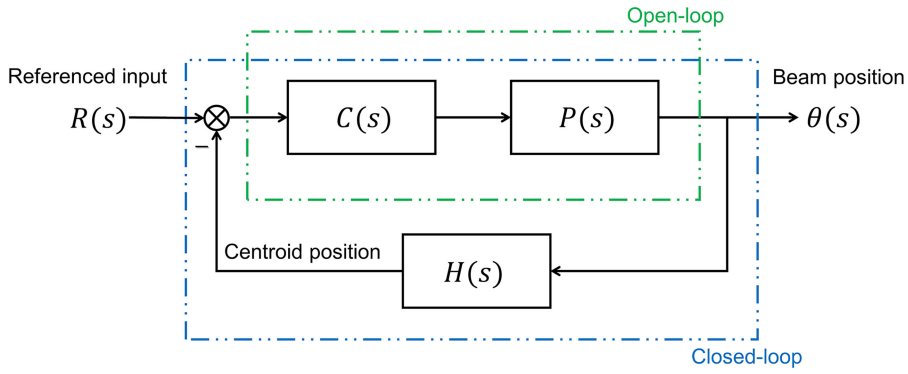

Fig. 6. Control structure for FSM. $R(s)$ is the referenced input; $C(s)$ is the controller; $P(s)$ presents the FSMs; $\theta(s)$ is the beam position; $H(s)$ is the centroid extracting algorithm. Since the centroid position obtained by algorithm is quite accurate, we assume $H\ (s) = 1$.

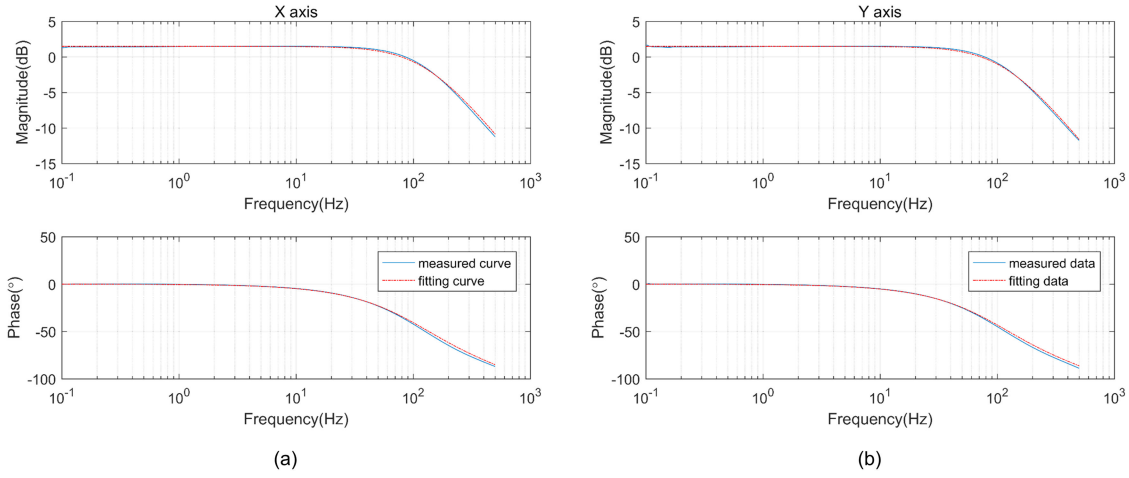

Fig. 7. The response characteristics of one FSM: (a) along X axis; (b) along Y axis. The blue curve represents the measured data, and the red curve is the fitting data.

in which case the referenced input $R(s)$ is the voltage value input by the operator, and the controller $C\ (s) = 1$. The blue part presents the closed-loop control, in which case the $R(s)$ is the referenced position, and the $C(s)$ is PID controller designed based on the fitting transfer function of FSM.

The response characteristics of all three FSMs are measured by a spectral analyzer from 0.1 Hz to 500 Hz, and one of which is shown in Fig. 7. The transfer function of the FSMs are therefore obtained by fitting the measurement data, and one of which is expressed as follows:

$$P_x\ (s) = \frac{1.187}{\frac{1}{780.64}s + 1} \times e^{-0.00005s} \tag{12}$$

$$P_y\ (s) = \frac{1.187}{\frac{1}{714.00}s + 1} \times e^{-0.00005s} \tag{13}$$

where $P_x(s)$ is the response characteristics along X axis, and $P_y(s)$ is the response characteristics along Y axis.

The ICU and the IPU are independently designed and manufactured. The schematic design of ICU and IPU and the corresponding relationship between their components and actual objects are shown in Fig. 8. The IPU contains a field programmable gate array (FPGA), a graphics processing

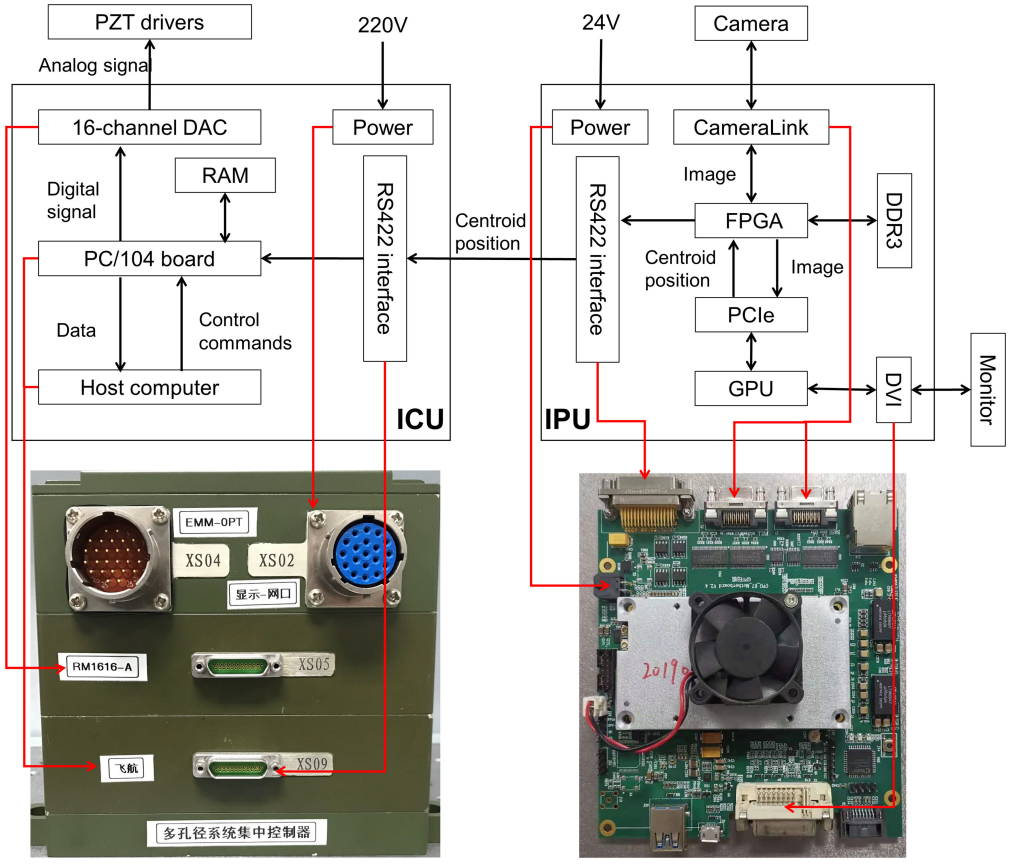

Fig. 8. The schematic design of ICU and IPU and the corresponding relationship between their components and actual objects.

unit (GPU) and a double data rate SDRAM (DDR3), as well as communication hardware, such as the CameraLink interface between the detection camera and the IPU, the PCIe capture card between the FPGA and the GPU, the DVI interface between the IPU and the monitor, and the RS422 interface between the ICU and the IPU. The types and characteristics of each component are shown as follows:

FPGA: XILINK Kintex-XC7K325T, 200 Gb/s max transceiver rate; DDR3: 256 MB, 1666 MHz; GPU: NVIDIA Jetson TX2, 2 GHz processing rate, 8GB LPDDR4 (1866 MHz).

The ICU connects a host computer, a digital-to-analog converter (DAC), a random access memory (RAM), and a RS422 interface for communicating with the IPU through the PC104 board. The DAC converts digital control commands from ICU into analog signals and sends them to the PZT drivers. This system has high positioning accuracy of the PZT ceramics, so a high-precision 16 bit DAC board is used. The output range of DAC is 0-10 V, so the resolution is $10/(2^{16}-1) = 0.15$ mV. Considering the influence of other circuit noise, the accuracy of the DA output can be controlled below 2 mV, and the corresponding positioning accuracy of FSM (2 mrad stroke) is about 40 nrad.

There are many components of the tip/tilt alignment module. In order to ensure that each unit can work together well, the software design is very important. The ICU runs a real-time software based on the Windows XP Embedded operating system with a sampling frequency of 1000 Hz. In order to facilitate debugging and monitoring, this real-time software has two layers, one is a real-time execution (RTX) software, and the other is a user interaction (UI) software. The RTX and the UI software communicate with each other by sharing variables. The operator can select whether the

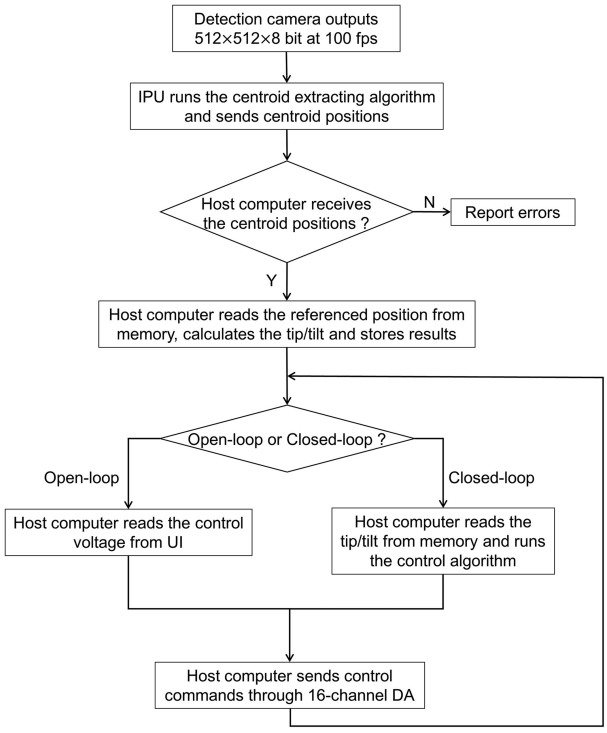

Fig. 9. Data processing flow.

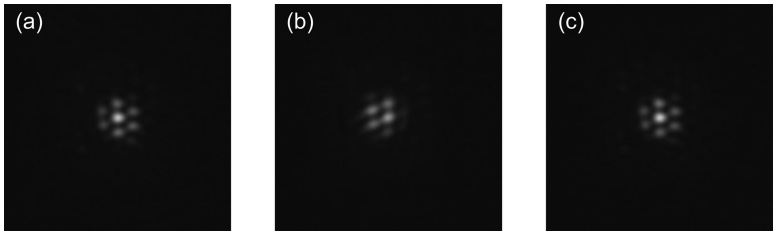

Fig. 10. Interference fringe (a) in the initial state; (b) in the open-loop manner after 5 min; (c) in the closed-loop manner.

system is operating in an open-loop manner or a closed-loop manner on the UI interface, and monitor the values of all variables at the same time. In the open-loop manner, the positions of the FSMs are directly determined by the voltage values that are input on the UI interface (0–10 V corresponds to 0-2 radians). In the closed-loop manner, the RTX runs the control algorithm (PID), according to the centroid positions sent by the centroid extracting algorithm in the IPU, thereby sending control commands to the PZT drivers for rotating FSMs in both directions. The detailed data processing flow is illustrated in Fig. 9.

5. Closed-loop Experiments

A series of experiments for a point source were conducted to demonstrate the practicability of TADS. The sub-telescopes were first manually aligned and phased together so that the three light spots on the science camera completely overlap and interfere with each other, as shown in Fig. 10(a). At the same time, the centroid positions of three sub-spots on the detection camera are recorded as referenced positions. When the ICU is working in an open-loop manner, the

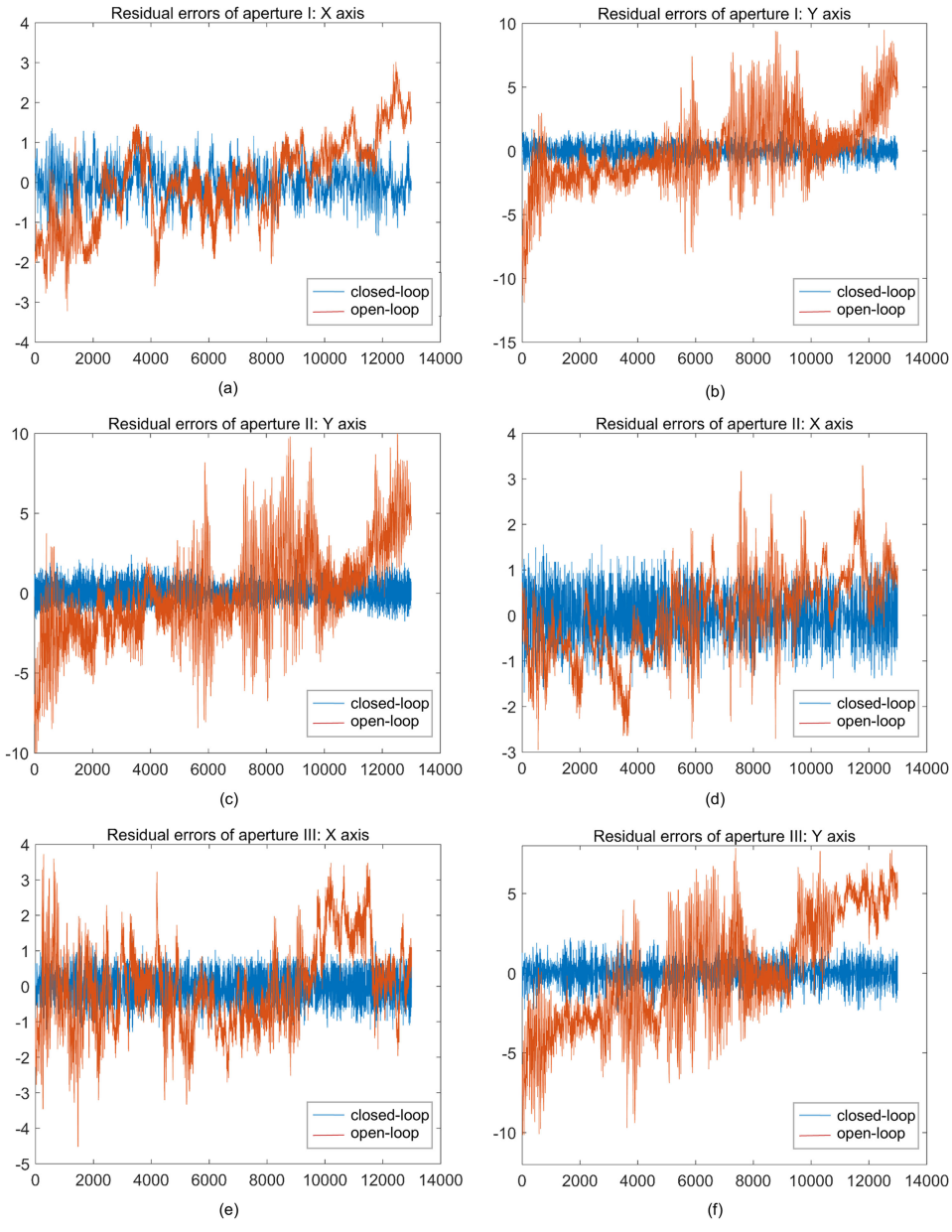

Fig. 11. Residual tip/tilt errors of three sub-telescopes: closed-loop v.s. open-loop.

TABLE 1
Residual tip/tilt errors RMS of three sub-telescopes, units in pixels

Sub-telescopes	Aperture I		Aperture II		Aperture III	
Directions	X axis	Y axis	X axis	Y axis	X axis	Y axis
Open-loop	1.0506	2.7601	0.9304	2.9039	1.1973	3.5007
Closed-loop	0.4234	0.5665	0.4534	0.5662	0.3663	0.7260

interference fringes on the science camera are degraded gradually after 5 min, as shown in Fig. 10(b). The degradation means the light spots do not completely overlap due to the tip/tilt that is caused by the air turbulence, the ground vibration, or the actuator creep. When the ICU is working in a closed-loop manner, the FSMs are driven to compensate the tip/tilt along X axis and Y axis automatically, so that the interference fringes on the science camera is kept almost the same as the initial state in Fig. 10(a), as shown in Fig. 10(c). The comparison of the open-loop fringes and the closed-loop fringes states that TADS conducts the tip/tilt alignment effectively.

In order to quantify the closed-loop performance, the residual tip/tilt errors of all three sub-telescopes in 13000 frames (130 seconds) on the detection camera are measured by the centroid extracting algorithm, as shown in Fig. 11. The red curves denote that the light spots dither severely in the open-loop manner. The blue curves indicate that the tip/tilt is effectively corrected in the closed-loop manner. Table 1 shows the root mean square (RMS) value of the residual tip/tilt errors. Compared with the open-loop manner, the tip/tilt is reduced by at least 51% (Aperture II: X axis), and by 81% (Aperture II: Y axis) sometimes in the closed-loop manner. The experiments prove that the proposed TADS can undoubtedly compensate the tip/tilt of sub-telescopes.

6. Conclusion

The Fizeau telescope array features a modular architecture to facilitate aperture expansion. As the prerequisite for the phased imaging, TADS has been used to regulate the tip/tilt for a Fizeau multi-aperture testbed with a point light source in our laboratory. The servo-control module drives the FSMs to rotate along two orthogonal axes. Based on TADS, the system can detect the tip/tilt with the centroid extracting algorithm no matter how many sub-telescopes are employed, so that the tip/tilt of each sub-telescope can be corrected separately at the same time. Besides, due to the simple structure consisting of two cameras and one beam splitter, TADS is easy to implement. A series of experiments demonstrate the performance of TADS. Compared with the open-loop manner, at least 51% reduction of the tip/tilt is achieved when the ICU is working in the closed-loop manner, which proves the feasibility of TADS. Simple and fast, the proposed tip/tilt alignment scheme is promising for Fizeau interferometric imaging.

References

[1] T. S. Mast and J. E. Nelson, "The status of the WM Keck observatory and ten meter telescope," in *Proc. SPIE*, 1986, pp. 0571 226–0571 232.
[2] G. M. Smith, "Keck II status report," in *Proc. SPIE*, 1997, pp. 2871 10–2871 14.
[3] G. H. Sanders, "The thirty meter telescope (TMT): An international observatory," *J. Astrophys. Astr.*, vol. 34, pp. 81–86, 2013.
[4] M. Dimmler *et al.*, "Getting ready for serial production of the segmented 39-meter ELT primary status, challenges and strategies," in *Proc. SPIE*, Art. no. 10700.
[5] M. Johns *et al.*, "Status of the giant magellan telescope (GMT) project," in *Proc. SPIE*, pp. 441–453, Art. no. 5489.
[6] P. A. Lightsey, "James webb space telescope (JWST): Optical performance of a large deployable cryogenic telescope," in *Proc.Conf. Lasers Electro-Optics*, pp. 1–2.
[7] A. D. Poyner, J. W. Montgomery, and B. L. Ulich, "MMT pointing and tracking," in *Proc. SPIE*, pp. 9–15, Art. no. 0628, 1986.
[8] J. S. Fender and R.A. Carreras, "Demonstration of an optically phased telescope array," *Opt. Eng.*, vol. 27, no. 9, pp. 706–711, 1988.
[9] C. R. DeHainaut, D. C. Duneman, R. C. Dymale, J. P. Blea, B. D. O'Neil, and C. E. Hines, "Wide field performance of a phased array telescope," *Opt. Eng.*, vol. 34, no. 3, pp. 876–880, 1995.
[10] S-J. Chung, D. W. Miller, and O. L. de Weck, "ARGOS testbed study of multidisciplinary challenges of future spaceborne interferometric arrays," *Opt. Eng.*, vol. 43, no. 9, pp. 2156–2167, 2004.
[11] R. L. Kendrick *et al.*, "Wide-field fizeau imaging telescope experimental results," *Appl. Opt.*, vol. 45, no. 18, pp. 4235–4240, 2006.
[12] Q. Wu, J. Fan, F. Wu, J. Zhao, and L. Qian, "Error analysis of the Golay3 optical imaging system," *Appl. Opt.*, vol. 52, no. 13, pp. 2966–2973, 2013.
[13] L. M. Mugnier, A. Blanc, and J. Idier, "Phase diversity a technique for wave-front sensing and for diffraction-limited imaging advances in imaging & electron physics," *Adv. Imag. Electron. Phys.*, vol. 141, pp. 1–76, 2006.
[14] M. Ni *et al.*, "The control system of a distributed aperture imaging testbed," *IEEE Trans. Control Syst. Technol.*, vol. 18, no. 6, pp. 1338–1344, 2010.

[15] M. G. Löfdahl, G. B. Scharmer, and W. Wei, "Calibration of a deformable mirror and strehl ratio measurements by use of phase diversity," *Appl. Opt.*, vol. 39, no. 1, pp. 94–103, 2000.
[16] J. J. Dolne, P. Meenicucci, D. Miccolis, and K. Widen, "Advanced image processing and wavefront sensing with real-time phase diversity," *Appl. Opt.*, vol. 48, pp. A30–A34, 2009.
[17] S. Vievard, F. Cassaing, and L. M. Mugnier, "Large amplitude tip/tilt estimation by geometric diversity for multiple-aperture telescopes," *J. Opt. Soc. Amer. A*, vol. 34, pp. 1272–1284, 2017.
[18] S. Vievard, F. Cassaing, A. Bonnefois, L. M. Mugnier, and J. Montri, "Real-time alignment and co-phasing of multi-aperture systems usingphase diversity," in *Proc. SPIE*, 2016, Art. no. 9906.
[19] S. Robbe *et al.*, "Active phase stabilization at the I2T: Implementation of the ASSI table," in *Proc. SPIE*, pp. 222–230, 1994, Art, no. 2200.
[20] S. Robbe, B. Sorrente, F. Cassaing, Y. Rabbia, and G. Rousset, "Performance of the angle of arrival correction system of the I2T + ASSI stellar interferometer," *Astron. Astrophys. Suppl. Ser.*, vol. 125 pp. 367–380, 1997.
[21] B. Sorrente, F. Cassaing, G. Rousset, and S. Robbe-Dubois, "Real-time optical path difference compensation at the plateau de calern I2T interferometer," *Astron. Astrophys.*, vol. 365, no. 2, pp. 301–313, 2001.
[22] M. Shao, M. M. Colavita, and D. H. Staelin, "The mark III astrometric interferometer," in *Proc. SPIE.*, vol. 0628, 1986, pp. 250–254.
[23] J. Xue, A. Jiang, S. Wang, and J. Wang, "Design and experimental demonstration of pointing correction module for a fizeau imaging interferometer," *Appl. Opt.*, vol. 57, no. 34, pp. 9936–9943, 2018.
[24] Z. Xie, H. Ma, X. He, and B. Qi, "Adaptive piston correction of sparse aperture systems with stochastic parallel gradient descent algorithm," *Opt. Express.*, vol. 26, no. 18, pp. 9541–9551, 2018.
[25] X. Ma, Z. Xie, H. Ma, Y. Xu, D. He, and G. Ren, "Piston sensing of sparse aperture systems with a single broadband image via deep learning," *Opt. Express*, vol. 27, no. 11, pp. 16058–16070, 2019.
[26] A. Cheetham, N. Cvetojevic, B. Norris, and A. Sivaramakrishnan, "Fizeau interferometric cophasing of segmented mirrors: Experimental validation," *Opt. Express*, vol. 22, no. 11, pp. 12924–12934, 2014.
[27] K. E. S. Ford *et al.*, "Active galactic nucleus and quasar science with aperture masking interferometry on the james webb space telescope," *Astrophys. J.*, vol. 783, no. 2, 2014, Art. no. 73.